Seismic imaging of upper-mantle structure with new evidence for a 520-km discontinuity

Peter M. Shearer

Institute of Geophysics and Planetary Physics, Scripps Institution of Oceanography, University of California, San Diego, La Jolla, California 92093, USA

Stacked images of long-period seismic data reveal many phases, some not previously observed, which are caused by reflections and conversions at discontinuities in the Earth's upper mantle. These images support the existence of discontinuities at 410, 520 and 660 km depth, but no evidence is found for a significant interface at 220 km.

SEISMIC velocities in the Earth's upper mantle increase more rapidly with depth than is to be expected from the increasing pressure alone, indicating that phase changes or differences in rock chemistry must be occurring. At some depths seismic properties change very rapidly, and relatively sharp discontinuities must be present. Although many possible discontinuity depths have been proposed, most recent models of upper-mantle structure contain discontinuities only near 400 and 670 km depth. An understanding of these seismic observations has been sought from high-pressure experiments in mineral physics, which suggest that the 400-km discontinuity is caused by the phase change between α- and β-olivine[1], and the 670-km discontinuity can be explained by the transformation γ-olivine (spinel) → perovskite + magnesiowüstite[2], although some researchers argue for chemical changes at these discontinuities[3]. These experiments have direct implications for the continuing controversy over whether the entire mantle has a relatively uniform composition in which discontinuities represent phase changes alone, or whether it is stratified into layers of different chemical composition. Seismology may help to resolve this dispute by providing more precise information on the strength, sharpness and possible topography of these discontinuities.

In addition to the well established major discontinuities near 400 and 670 km, there is some seismic evidence for other upper-mantle discontinuities. Numerous studies[4–8] have found evidence for a discontinuity or steep velocity increase near 220 km, leading some to suggest that a 220-km discontinuity is an important global feature which occurs beneath both oceans and continents[7]. Proposed explanations for a 220-km discontinuity have included a composition change between garnet lherzolite and eclogite[7] and the existence of an anisotropic layer caused by preferred alignment of olivine crystals[8]. But many recent seismic studies[9,10] of upper-mantle structure are inconsistent with a significant discontinuity at 220 km, so it is unclear how globally coherent such a feature can be. A small number of studies have also suggested a discontinuity or enhanced velocity gradient at 520 km depth[5,11–17] which may be associated with the β-olivine → spinel phase change[1]. Discontinuities at various other depths have been proposed as well[5,11,12], but with little consensus between different studies regarding their occurrence.

Seismic evidence for discontinuities in the upper mantle began with the recognition of a sharp bend in the P wave travel-time curve near 20° range[18,19], and has continued with detailed travel-time and synthetic seismogram analyses of both P and S wave phases[9,10,20]. Other evidence for upper-mantle discontinuities has come from observations of secondary arrivals resulting from topside reflections[11,21–26], bottomside reflections[21,26–32] and phase conversions between P and S at the discontinuities[33–41]. Again, many different discontinuity depths have been suggested by these observations, with general agreement occurring only for the 400- and 670-km discontinuities. Most of these studies of secondary arrivals have concentrated on examining data from a relatively small number of earthquakes and seismic stations, often with poor signal-to-noise characteristics, and it is not always clear which features of the models are global in nature and which may be peculiar to a particular region or data set.

The current availability of large seismic data sets in digital form makes it practical to 'stack' and average thousands of seismograms to remove the effects of local structure and enhance the visibility of weak global seismic phases. Here I present the results of stacking five years of long-period seismic data from the Global Digital Seismograph Network (GDSN). Images resulting from these stacks clearly show many phases related to upper-mantle discontinuities; some of these phases have not previously been observed. Strong phases are seen associated with discontinuities at apparent depths of about 410 and 660 km. Depths calculated for individual stations agree to within 20 km of these values, suggesting a possible limit to the amplitude of any topography on these discontinuities. In addition, these images appear to show two seismic phases from a discontinuity at 520 km depth, thus supporting the results of earlier studies which have indicated structure at or near this depth[5,11–17]. No evidence is found for a 220-km discontinuity, although phases associated with such a discontinuity should be visible in some of the stacked images if the 220-km discontinuity were a significant global feature.

Stacking long-period seismograms

For more than ten years, seismograms from the Global Digital Seismograph Network (GDSN) have been available through the National Earthquake Information Center at the United States Geological Survey. This study uses data only from the five years (1980–1984) that are currently available on optical disk (CD-ROM), the most convenient form for automatic processing of large parts of the data set. These five years contain records for 1,827 earthquakes and nuclear explosions, with an average of about 21 stations per event, for a total of 38,578 event-station pairs.

My analysis is limited to the long-period GDSN data, which record three components (vertical and two horizontals) sampled at 1 Hz, filtered such that the seismic pulses recorded have a dominant period of about 20 s. Long-period seismic data are particularly suited for stacking (the addition of different seismic records to yield a single composite record with higher signal-to-noise ratio) because of the coherence and simplicity of typical long-period waveforms. The stacking procedure works in the following way: (1) The analysis is restricted to events shallower than 50 km to eliminate complications owing to depth phases (surface reflections near the source). (2) The amplitude and start time of each seismogram are normalized with respect to a reference seismic phase. This procedure increases the coherence

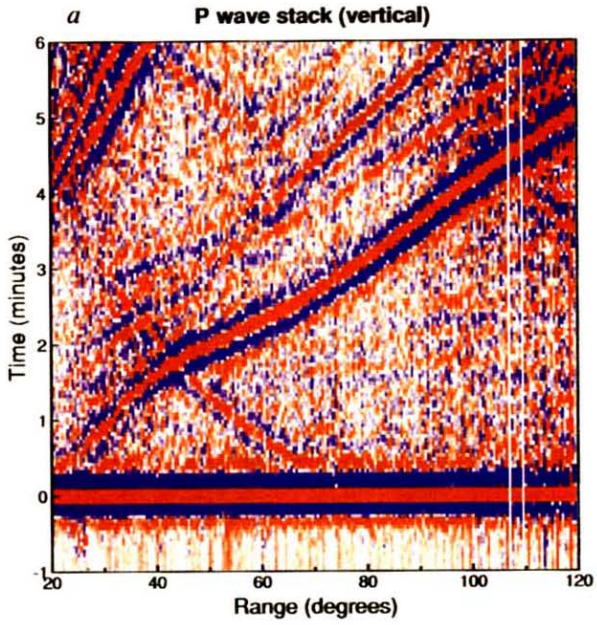
a
P wave stack (vertical)
Time (minutes)
Range (degrees)

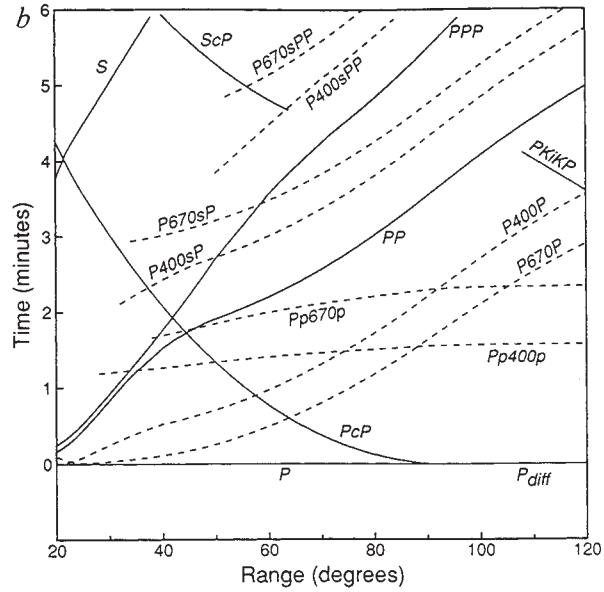
b
S
ScP
P670sPP
P400sPP
PPP
PKiKP
P670sP
P400sP
PP
P400P
P670P
Pp670p
Pp400p
PcP
P
Pdiff
Time (minutes)
Range (degrees)

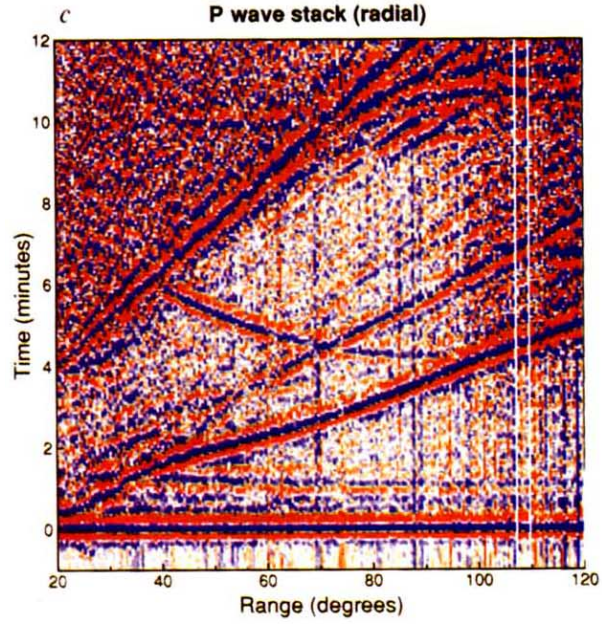
c
P wave stack (radial)
Time (minutes)
Range (degrees)

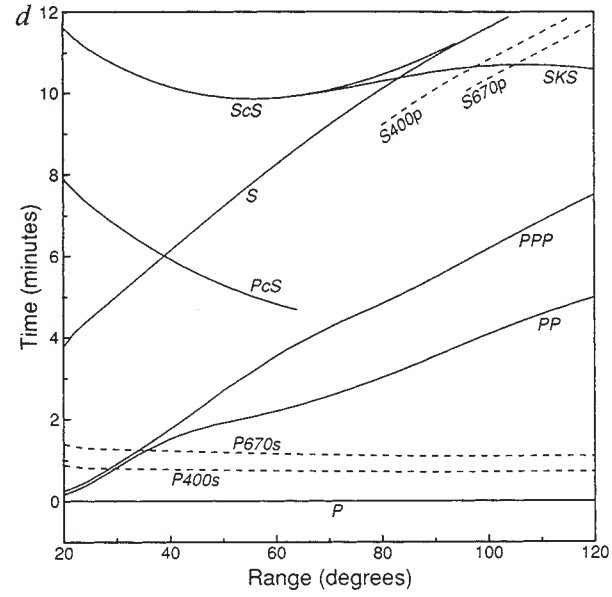
d
ScS
S400p
S670p
SKS
S
PcS
PPP
PP
P670s
P400s
P
Time (minutes)
Range (degrees)

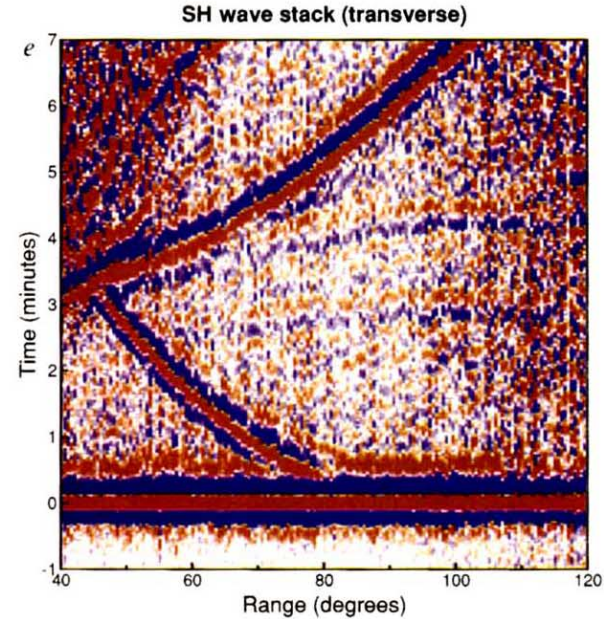
SH wave stack (transverse)
e
Time (minutes)
Range (degrees)

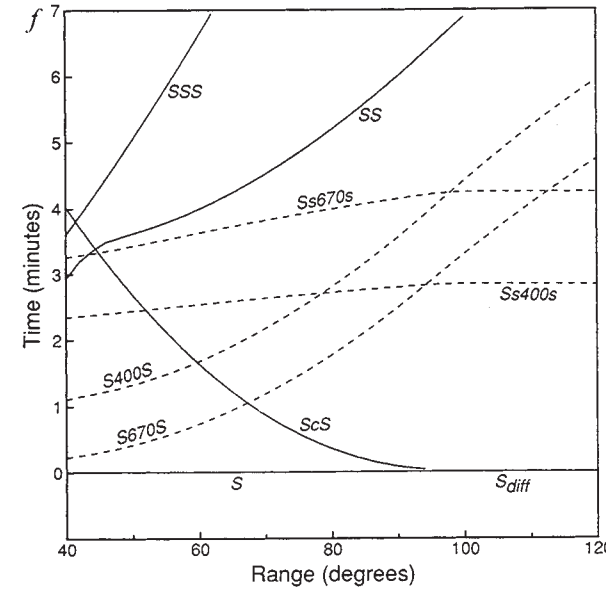
f
SSS
SS
Ss670s
Ss400s
S400S
S670S
ScS
S
Sdiff
Time (minutes)
Range (degrees)

◀ FIG. 1 Stacked colour images of long-period GDSN data compared with travel-times curves for primary seismic phases (solid) and upper-mantle discontinuity phases (dashed). Positive amplitudes are shown in red, negative amplitudes in blue, with the scale ranging up to 0.1 of the maximum amplitude of the reference phase. The stacks include: *a, b,* P wave reference phase, vertical-component stack; *c, d,* P wave reference phase, radial-component stack; *e, f,* SH wave reference phase, transverse-component stack. Note the apparent phases visible in *a* between Pp400p and Pp670p, and in *e* between Ss400s and Ss670s, representing possible reflections off a 520-km discontinuity.

of the stack and reduces the effects of differing source functions and instrument responses and errors in earthquake depths and origin times. Both P wave and SH wave reference arrivals are used in the stacks shown here. (3) The maximum amplitude in the seismogram is found within 60-s windows both preceding and following the theoretical arrival time of the reference phase. These amplitudes are used as a measure of the size of the 'noise' level before the reference phase arrival and of the 'signal' contained in the reference phase. The seismogram is discarded if the signal-to-noise ratio is less than 10. This ensures that only the higher-quality data are used in the stack. (4) The amplitude scaling and start time of each seismogram are adjusted such that the maximum amplitude of the reference phase is unity at zero time. The polarity of the seismogram is switched if necessary. This has the effect of aligning the peaks in the reference phase for all the seismograms in the stack. In general, the waveform shapes in the reference pulses will not be the same, mainly because of differences in event depths. When applied to dozens of events, however, this stacking procedure results in an effective source function that is peaked as sharply as possible. (5) Values obtained from each trace are averaged within bins of range and travel time to produce a stacked record section combining all the data.

These stacked images are seen most clearly on displays in which positive and negative amplitudes are represented with different colours so that the polarity and phase of the various seismic arrivals can be seen directly.

P wave stack (vertical component)

Figure 1*a* shows the result of aligning the P wave arrival and stacking on the vertical component at ranges between 20° and 120° and travel times of up to 6 min following the P wave arrival. The data are binned and averaged in increments of 0.5° in range and 3 s in time. 2,332 seismograms are stacked from 35 stations, for an average of about 12 seismograms per range bin. Positive amplitudes are shown in red, negative amplitudes in blue. Note that the P wave arrival has been aligned at zero time, and the maximum amplitudes shown are only one tenth the size of the P wave amplitude. This enhances the appearance of the weaker seismic phases, at the expense of 'clipping' the strong arrivals. At ranges beyond about 95°, the P wave has been diffracted around the core-mantle boundary, corresponding to the ray path labelled P_{diff} in Fig. 2. P_{diff} is a weaker phase than direct P, reducing the number of good-quality records available for stacking. This causes the stack to become noticeably noisier at ranges beyond 100°, because of the smaller numbers of traces at these ranges. The two white vertical lines towards the right of the plot are the result of the absence of data within two individual range bins.

Figure 1*b* shows theoretical differential travel times calculated by tracing rays through PREM[42], a reference Earth model. Major phases are shown as solid lines; these include P, PP, PPP, PcP, PKiKP, S and ScP (Fig. 2 shows the geometry for many of these phases). The phase of a particular seismic arrival can be identified by its colour pattern. For example, the blue-red-blue pattern of the core-reflected phase PcP indicates that it has not been phase-shifted relative to the direct P arrival. By contrast, the red-blue-red-blue pattern of the surface-reflected phase PP shows the $\pi/2$ phase shift (the Hilbert transform) known to occur for this phase[43].

The dashed lines show some of the upper-mantle discontinuity phases discussed in this paper. Figure 3 shows examples of ray paths for these phases. Perhaps most visible are the two phases P400sP and P670sP, which follow PP and contain a single S leg between the 400- and 670-km discontinuities and the surface ('400' and '670' will be used in the phase names and discussion, although the actual discontinuity depths may be slightly different). These phases can be followed from a range of 30° to 120°. Figure 3*a* shows only one of the four possible geometries for these phases; the S leg could replace any of the P legs shown and the same travel time would result. Analogous to these phases are the arrivals that follow PPP (namely, P400sPP and P670sPP) which also contain a single S leg between the discontinuities and the surface. These phases are visible beyond about 50°.

Weak phases can be seen following the direct P wave arrival by about 1.5 to 2.5 min at ranges between 70° and 120°. These are P wave multiples (Pp400p and Pp670p) which result from topside reflections off upper-mantle discontinuities[21–25]. Notice that they are phase-reversed relative to the P wave, a result of the surface reflection. An apparent phase can be seen between the Pp400p and Pp670p arrivals. The position of this phase corresponds to a topside reflection from a 520-km discontinuity (that is, to Pp520p). An analogous phase appears in the SH wave stack and will be discussed later. Also shown in Fig. 1*b* are travel-time curves for the bottomside reflected phases P400P and P670P which precede PP (refs 21, 25, 28, 29). These phases are visible only marginally in the stacked image, most clearly between 90° and 110°. Noticeably absent in Fig. 1*a* is any indication of a multiple from a 220-km discontinuity (Pp220p), which would appear between P and Pp400p.

P wave stack (radial component)

Figure 1*c* shows the result of stacking on the radial horizontal seismometer component after aligning the P wave arrival as in the previous example. The binning increments are the same but results are displayed out to 12 min to show some of the details near the S wave arrival. The maximum amplitude shown is 0.1 of the P wave amplitude. Figure 1*d* shows differential travel times for the phases visible in this stack. These include P, PP, PPP, PcS, S, ScS and SKS. Note that PcS is visible out to 90°, well beyond the ray theoretical limit for this phase. At ranges between 65° and 90°, this phase is actually PcS_{diff}, with the P wave diffracting around the core-mantle boundary (see Fig. 2).

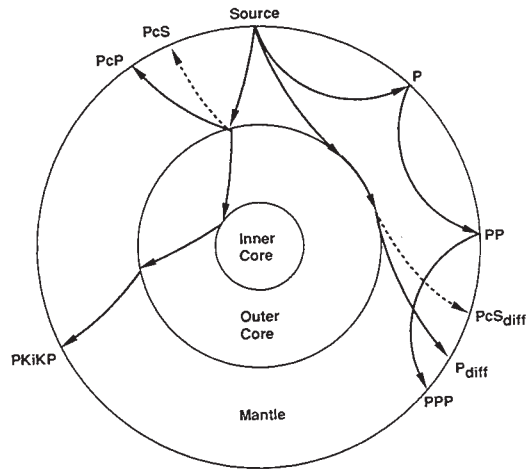

FIG. 2 Schematic of the major global seismic phases seen in Fig. 1. The phases are associated with interactions with three discontinuities: the surface, the core–mantle boundary, and the inner-core boundary. Compressional waves (P) are shown as solid lines; shear waves (S) are shown as dashed lines. Reflections are indicated with lower-case letters; for example, PcP is the P wave which is reflected off the core–mantle boundary, and PKiKP is reflected from the inner-core boundary. P_{diff} and PcS_{diff} are phases that have been diffracted around the core–mantle boundary.

Preceding the S arrival are two phases, S400p and S670p, that result from SV to P conversions at the 400-km and 670-km discontinuities beneath the station (see Fig. 3)[34,37,38,41]. These arrivals may also contain energy from P to SV conversions at discontinuities below the events (p400S and p670S); these phases arrive at the same time as the SV-to-P converted phases, and both sets of arrivals are seen most clearly on the radial component[37]. S400p and S670p can be seen at ranges as small as 60° and 80° respectively, much closer than the ray theoretical limits shown in Fig. 1*d* but in agreement with the results of synthetic seismogram modelling[34].

Two phases—P400s and P670s—can be seen clearly as blue streaks in Fig. 1*c*, which follow the direct P by about 40 s to 90 s. These result from P to SV conversions at discontinuities below the recording stations[33,39,40]. The time separation between these phases is too short to permit a 520-km discontinuity to be seen, because the dominant period of the pulses is about 20 s. The blue streak visible between P and P400s is a sidelobe artefact of direct P, as it remains parallel to P even at short ranges, whereas a converted phase from a discontinuity shallower than 400 km would become increasingly delayed at close ranges. Also visible in Fig. 1*c* are hints of the discontinuity phases which can be seen more clearly in the vertical-component stack (Fig. 1*a*).

SH wave stack (transverse component)

Figure 1*e* shows the result of aligning the SH wave and stacking on the transverse horizontal component at ranges between 40° and 120° and travel times of up to 7 min following the SH wave arrival. The data are binned and averaged in increments of 0.5° in range and 2 s in time. 2,648 seismograms are stacked from 35 stations, for an average of about 17 seismograms per range bin. As in the P wave stacks, the image becomes noisier at ranges beyond about 100° because of the relatively small number of good-quality S_{diff} arrivals in these ranges. Figure 1*f* shows travel times for seismic phases visible in the transverse-component stack. The S, SS, SSS and ScS phases are seen clearly. As expected[43], the SS phase is Hilbert-transformed relative to S.

Also clearly apparent in this stack are the SH wave multiples resulting from topside reflections off the 400-km and 670-km discontinuities (Ss400s and Ss670s; see Fig. 3). These are phase-reversed relative to S and are visible between about 70° and 115°. As in the case of the P wave multiples, a phase also appears between these reflections which is apparently caused by a discontinuity at about 520 km depth. This feature is better resolved in the SH stack because of the relatively large time separation between the Ss400s and Ss670s arrivals. I will discuss later the implications of this phase. Figure 1*e* also shows travel times for the bottomside reflected phases S400S and S670S, which precede SS. These phases can be seen only faintly in the stacked image. As in the case of the P wave stack, there is no visible phase corresponding to a multiple off a 220-km discontinuity.

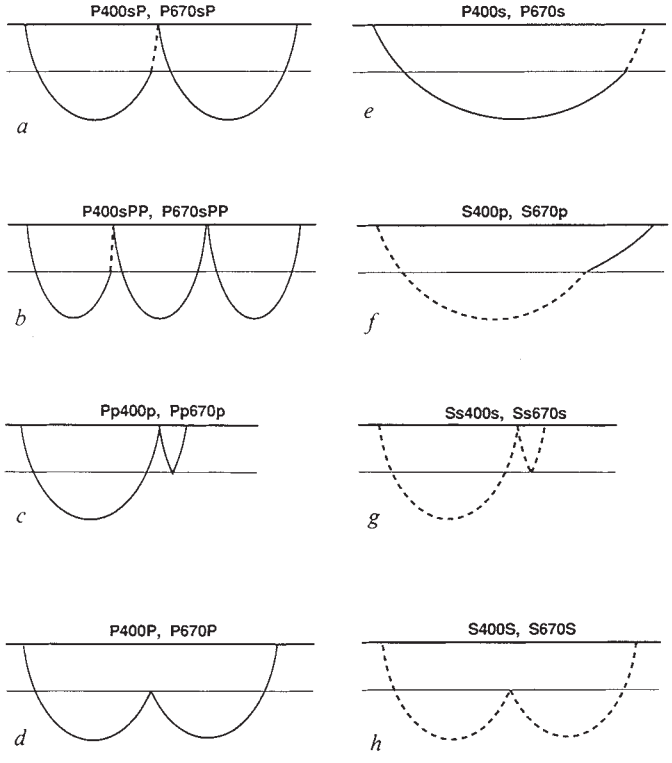

FIG. 3 The secondary seismic phases visible in Fig. 1, which are associated with reflections and conversions at upper-mantle discontinuities. P waves are shown as solid lines and S waves as dashed lines, with the thin horizontal line representing either the 400- or the 670-km discontinuity. Lower-case p and s represent short ray segments between the discontinuities and the surface. Phases *a*–*d* can be seen most clearly on the vertical-component stack, *e* and *f* most clearly on the radial-component stack, and *g* and *h* on the transverse-component stack.

Cross-correlation analysis

As an alternative to the stacking procedure discussed above, a cross-correlation method can be used to resolve upper-mantle discontinuity phases. This has the advantage of permitting the computation of discontinuity depths for each seismogram individually to see if these results are consistent with the stacked images. The cross-correlation analysis proceeds as follows: (1) The same seismograms are used as in the stacking method, that is, those from events shallower than 50 km and with signal-to-noise ratios of ten or better. (2) For each reference phase (P or SH), a 41-s wavelet centred on the maximum-amplitude point is used as a reference waveform and the cross-correlation function between this wavelet and the rest of the seismogram is computed. (3) Peaks in the cross-correlation function are identified and saved. This procedure finds the time shifts to pulses in the seismogram that are similar in shape to the reference arrival and which may thus represent other phases. (4) Assuming a particular discontinuity phase of interest and an upper-mantle velocity model, these points may be converted directly into discontinuity depths.

Figure 4 shows the results of this procedure applied to the 2,648 seismograms in the SH wave stack. To resolve the SH wave multiples from upper-mantle discontinuities, points are plotted only if the correlation coefficient, r, between the reference wavelet and the seismogram is less than -0.7 (the correlation coefficient is negative because these arrivals are phase-reversed relative to S). Both Ss400s and Ss670s are visible in this plot, as well as the apparent Ss520s multiple seen in the stacked image. Using an upper-mantle velocity model (such as PREM[42]), discontinuity depths can be calculated for each point in this plot.

Figure 5 shows the discontinuity depths predicted by cross-correlation analysis, using three different types of discontinuity phases and assuming PREM for the upper-mantle velocities. These phases include P to SV conversions recorded on the radial component between ranges of 40° and 105°, and P wave and SH wave multiples between 70° and 110° recorded on the vertical and transverse components, respectively. The vertical-component P wave is used as the reference wavelet for both the vertical- and radial-component analyses. Points are plotted only for $r > 0.7$ (or $r < -0.7$ for phase-reversed arrivals), and are binned in 20-km depth increments. Calculated average depths to the 400-km discontinuity are 411 km for P400s, 411 km for Pp400p and 415 km for Ss400s. Calculated depths to the 670-km discontinuity are 674 km for P670s, 660 km for Pp670p and 653 km for Ss670s. Depths to the 520-km discontinuity are 520 km and 519 km for Pp520p and Ss520s respectively. These depths depend on the velocity in the upper mantle above the discontinuities: slower velocities imply deeper discontinuities.

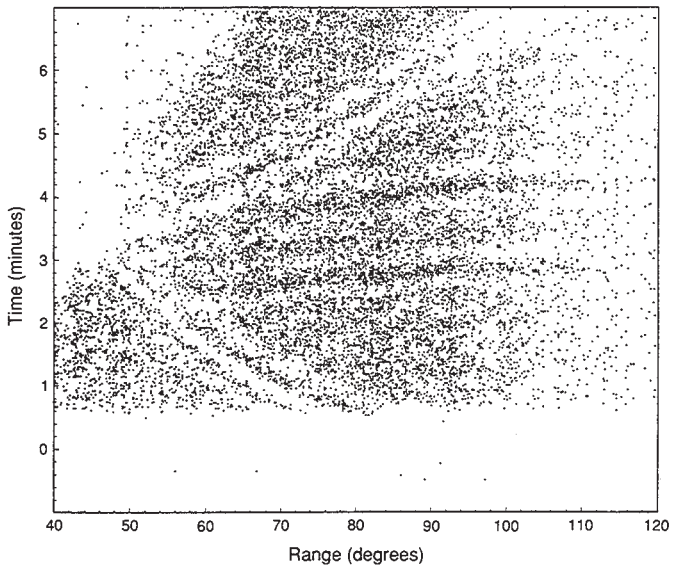

FIG. 4 Cross-correlation peaks for SH wave data (compare with Fig. 1*e*). The correlation coefficient, *r*, for each peak is less than −0.7, in order to resolve the phase-reversed reflections off the top of the upper-mantle discontinuities.

Assuming fixed upper-mantle velocities, uncertainties in these depths are ~10–20 km; a more formal error analysis is in progress.

As discussed previously, there is no possibility of resolving a 520-km discontinuity in long-period P-to-SV converted arrivals, given the small time separation between the 400-km and 670-km phases. There is no clear evidence for a discontinuity at 220 km depth for any of these converted phases. The P and S wave multiples suggest the possible presence of a discontinuity at ~840 km depth. The P wave stack (Fig. 1*a*) shows a hint of a possible Pp840p phase, but no corresponding S wave multiple can be seen in the SH wave stack (Fig. 1*e*).

Discussion

These stacks do not show any phases that can be associated with a discontinuity at 220 km depth. This is consistent with many upper-mantle models, which do not have significant structure at this depth[9,10]. Other models, however, do contain large discontinuities at 220 km, and in some areas the evidence for structure near this depth is quite strong[5,6]. PREM contains P and S wave impedance contrasts at 220 km that are roughly comparable in size to the contrasts at 400 km. Given that P wave and S wave multiples from the 400-km discontinuity are easily visible in these stacks, a 220-km discontinuity of comparable magnitude should also be seen. The absence of visible 220-km discontinuity phases indicates that the impedance contrast at 220 km must be significantly less than the PREM values or that the 220-km discontinuity is not a globally coherent feature. These results are consistent with recent analysis of ScS multiples which also fails to find evidence for a 220-km discontinuity[26].

The fact that 400-km and 670-km discontinuity phases can be seen so clearly in stacked images of global seismic data sets indicates that depths to these discontinuities cannot vary too widely between regions, because otherwise the coherence of the stack would be lost. Results obtained from cross-correlation analyses of records from individual seismic stations generally indicate discontinuity depth variations of less than ±20 km. Amplitudes of the Ss400s and Ss670s phases in the stacked record section are about 30% smaller than those predicted by the PREM model. This may indicate that the PREM S wave impedance contrast is too large at these discontinuities or it may be a result of slight differences in the discontinuity depths or lateral velocity variations which cause time shifts and partial cancellation of the pulses during the stacking procedure[26].

Both the P wave and S wave stacks suggest the presence of phases resulting from reflections off a 520-km discontinuity, with an apparent amplitude roughly half the size of the 400-km discontinuity phases. However, because these phases occur between the 400-km and 670-km multiples, the possibility must be considered that they are artefacts from the sidelobes of these phases. Detailed synthetic seismogram analysis will be necessary to resolve this question, but several factors suggest that these 520-km phases are real. These include: (1) The 520-km phases are not centred between the 400- and 670-km phases, but are closer in time to the 400-km phases. The time separation is too great for them to be considered sidelobes of the 670-km phases. (2) The 520-km phases follow the 400-km phases, but no corresponding phases follow the 670-km phases. (3) Cross-correlation analyses of the Pp520p and Ss520s phases give the same apparent depth for the 520-km discontinuity despite the different time separation between the 400-, 520- and 670-km multiples, because of the different velocities of P and S. (4) The amplitude of the Ss520s phase is over half the amplitude of the Ss400s phase—too large to be a sidelobe artefact of the 400-km phase, as the positive sidelobes of S are only about 15% of the size of the main S pulse in these stacked records. (5) The waveform of the stacked SS pulse shows no significant change from direct S (after Hilbert-transforming), indicating that the additional crustal transits have had little effect on the waveform. (6) Preliminary analysis of SH synthetic seismograms (toroidal mode sum) computed for PREM indicates no waveforms that could be mistaken for Ss520s.

Most recent upper-mantle velocity models do not have

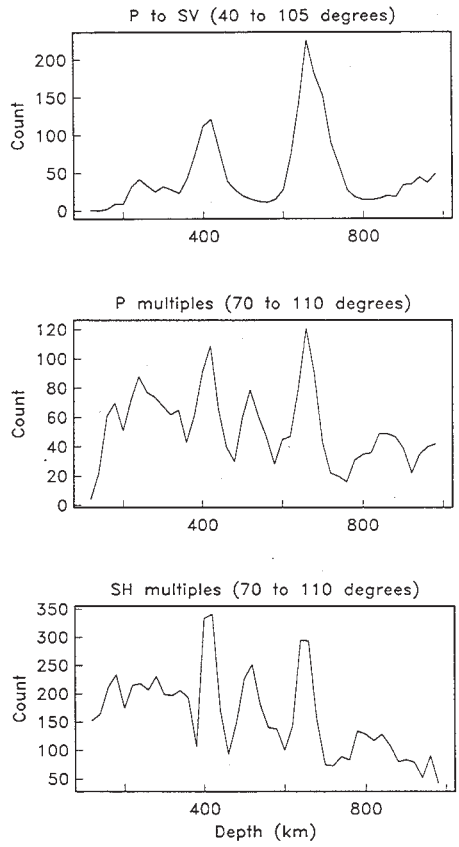

FIG. 5 Number of cross-correlation peaks as a function of discontinuity depths for P-to-SV converted waves (top), P wave multiples (middle), and SH wave multiples (bottom). Results have been binned in increments of 20 km in depth. The P and S multiples suggest the presence of a discontinuity at about 520 km depth.

significant structure near 520 km depth[9,10,42], although several older velocity models do contain discontinuities or kinks near this depth[5,13–17]. These models were based mainly on analyses of P and SH wave refraction data and P wave slowness data recorded at arrays. These types of analyses cannot distinguish between sharp velocity discontinuities and local regions of steep velocity gradients. The long-period data shown in this paper also cannot distinguish between a discontinuity or enhanced velocity gradient at 520 km. The amplitude of the apparent Pp520p and Ss520s phases discussed in this paper are consistent with an impedance contrast at 520 km of ~3%, occurring within a gradient region less than about 25 km thick. But there is also some evidence for a 520-km reflector from quarry blast explosions[11] and short-period precursors to the phase P'P' (ref. 12). If these observations do represent reflections of high-frequency energy off a 520-km discontinuity, then the discontinuity must be relatively sharp (less than ~4 km thick), just as other short-period P'P' precursors imply a locally sharp 670-km discontinuity[44,45].

It is tempting to explain the possible existence of a 520-km discontinuity as representing the phase change between β-olivine and spinel, which occurs at about the right depth[1,12]. Recent high-pressure laboratory results, however, suggest that the change in velocity associated with this phase change occurs gradually and is quite small[46]. Other suggestions for possible phase changes near 520 km have included enstatite → spinel + stishovite[12] and garnet → garnet + perovskite[1], with more recent laboratory results indicating many complicated phase changes in the pyroxene/garnet system[47]. In general, predicted upper-mantle phase changes are highly dependent on composition and temperature, so conclusively identifying a specific phase change may be difficult. □

Received 30 November 1989; accepted 26 January 1990.

1. Ringwood, A. E. *Composition and Petrology of the Earth's Mantle* (McGraw-Hill, New York, 1975).
2. Ito, E. & Takahashi, E. *J. geophys. Res.* **94,** 10637–10646 (1989).
3. Anderson, D. L. & Bass, J. D. *Nature* **320,** 321–328 (1986).
4. Lehmann, I. *Ann. Geophys.* **15,** 93–118 (1959).
5. Hales, A. L., Muirhead, K. J. & Rynn, J. M. W. *Tectonophysics* **63,** 309–348 (1980).
6. Drummond, B. J., Muirhead, K. J. & Hales, A. L. *Geophys. J. R. astr. Soc.* **70,** 67–77 (1982).
7. Anderson, D. L. *J. geophys. Res.* **84,** 7555–7560 (1979).
8. Leven, J. H., Jackson, I. & Ringwood, A. E. *Nature* **289,** 234–239 (1981).
9. Walck, M. C. *Geophys. J. R. astr. Soc.* **76,** 697–723 (1984).
10. Grand, S. P. & Helmberger, D. V. *Geophys. J. R. astr. Soc.* **76,** 399–438 (1984).
11. Hoffman, J. P., Berg, J. W. & Cook, K. L. *Bull. seismol. Soc. Am.* **51,** 17–27 (1961).
12. Whitcomb, J. H. & Anderson, D. L. *J. geophys. Res.* **75,** 5713–5728 (1970).
13. Helmberger, D. & Wiggins, R. A. *J. geophys. Res.* **76,** 3229–3245 (1971).
14. Wiggins, R. A. & Helmberger, D. V. *J. geophys. Res.* **78,** 1870–1880 (1973).
15. Helmberger, D. V. & Engen, G. R. *J. geophys. Res.* **79,** 4017–4028 (1974).
16. Simpson, D. W., Mereu, R. F. & King, D. W. *Bull. seismol. Soc. Am.* **64,** 1757–1788 (1974).
17. Fukao, Y. *Geophys. J. R. astr. Soc.* **50,** 621–642 (1977).
18. Byerly, P. *Bull. seismol. Soc. Am.* **16,** 209–265 (1926).
19. Jeffreys, S. H. *Mon. Not. R. astr. Soc. Geophys. Suppl.* **3,** 401–422 (1936).
20. Johnson, L. R. *J. geophys. Res.* **72,** 6309–6325 (1967).
21. Nguyen-Hai *Ann. Geophys.* **15,** 285–346 (1963).
22. Husebye, E. & Madariaga, R. *Bull. seismol. Soc. Am.* **60,** 939–952 (1970).
23. Davies, D., Kelly, E. J. & Filson, J. R. *Nature* **232,** 8–13 (1971).
24. Gutowski, R. R. & Kanesewich, E. R. *Geophys. J. R. astr. Soc.* **36,** 21–32 (1974).
25. Ward, S. N. *Bull. seismol. Soc. Am.* **68,** 133–153 (1978).
26. Revenaugh, J. & Jordan, T. H. *J. geophys. Res.* **94,** 5787–5813 (1989).
27. Engdahl, E. R. & Flinn, E. A. *Science* **163,** 177–179 (1969).
28. Bolt, B. A. *Geophys. J. R. astr. Soc.* **20,** 367–382 (1970).
29. Adams, R. D. *Bull. seismol. Soc. Am.* **61,** 1441–1451 (1971).
30. Husebye, E. S., Haddon, R. A. W. & King, D. W. *J. Geophys.* **43,** 535–543 (1977).
31. Nakanishi, I. *Geophys. J.* **93,** 335–346 (1988).
32. Davis, J. P., Kind, R. & Sacks, I. S. *Geophys. J.* **99,** 595–604 (1989).
33. Vinnik, L. P. *Phys. Earth planet. Inter.* **15,** 39–45 (1977).
34. Faber, S. & Müller, G. *Bull. seismol. Soc. Am.* **70,** 487–508 (1980).
35. Barley, B. J., Hudson, J. A. & Douglas, A. *Geophys. J. R. astr. Soc.* **69,** 159–172 (1982).
36. Bock, G. & Ha, J. *Geophys. J. R. astr. Soc.* **77,** 593–615 (1984).
37. Faber, S. & Müller, G. *J. Geophys.* **54,** 183–194 (1984).
38. Baumgardt, D. R. & Alexander, S. S. *Bull. seismol. Soc. Am.* **74,** 1683–1702 (1984).
39. Kind, R. & Vinnik, L. P. *J. Geophys.* **62,** 138–147 (1988).
40. Paulssen, H. *J. geophys. Res.* **93,** 10489–10500 (1988).
41. Bock, G. *J. Geophys.* **64,** 73–81 (1988).
42. Dziewonski, A. M. & Anderson, D. L. *Phys. Earth planet. Inter.* **25,** 297–356 (1981).
43. Choy, G. L. & Richards, P. G. *Bull. seismol. Soc. Am.* **65,** 55–70 (1975).
44. Richards, P. G. *J. Geophys.* **38,** 517–527 (1972).
45. Lees, A. C., Bukowinski, M. S. T. & Jeanloz, R. *J. geophys. Res.* **88,** 8145–8159 (1983).
46. Weidnor, D. J., Sawamoto, H., Sasaki, S. & Kumazawa, M. *J. geophys. Res.* **89,** 7852–7860 (1984).
47. Jeanloz, R. & Thompson, A. B. *Rev. Geophys. Space Phys.* **21,** 51–74 (1983).

ACKNOWLEDGEMENTS. I thank J. Garmany, G. Masters and G. Nolet for advice regarding this work. This research was partially supported by the NSF.

In vivo alteration of telomere sequences and senescence caused by mutated *Tetrahymena* telomerase RNAs

Guo-Liang Yu, John D. Bradley, Laura D. Attardi & Elizabeth H. Blackburn*

Department of Molecular and Cell Biology, University of California, Berkeley, California 94720, USA

Mutating the CAACCCCAA sequence in the RNA component of telomerase causes the synthesis *in vivo* of new telomere sequences corresponding to the mutated RNA sequence, demonstrating that the telomerase contains the template for telomere synthesis. These mutations also lead to nuclear and cell division defects, and senescence, establishing an essential role for telomerase *in vivo*.

TELOMERES, the ends of eukaryotic chromosomes, are essential for the stabilization of linear chromosomes and the completion of chromosomal DNA replication[1,2]. Telomeres from diverse eukaryotes, including protozoans, yeasts, plants and mammals, consist of simple tandemly repeated G+C-rich sequences, with the G-rich sequence at the 3′ end of each DNA strand of a chromosome[2–5]. For example, the telomeric sequence of the ciliated protozoan *Tetrahymena thermophila* consists of TTGGGG·AACCCC repeats[6].

The G-rich strand of telomeric DNA is synthesized *in vitro* by telomerase[7], a ribonucleoprotein enzyme with an essential RNA component[8,9]. The *Tetrahymena* telomerase synthesizes repeats of the telomeric DNA sequence 5′-TTGGGG-3′ without requiring an added exogenous template[7–9]. Analogous telomerase activities have been identified in the ciliates *Oxytricha nova*[10] and *Euplotes crassus*[11], and recently in human (HeLa) cells[12]; each synthesizes its species-specific repeats onto the 3′ end of a telomeric sequence using the G-rich sequence as a primer.

Telomerase activity, originally proposed on the basis of *in vivo* studies of heterologous telomeres in yeast, readily explains

* To whom correspondence should be addressed.